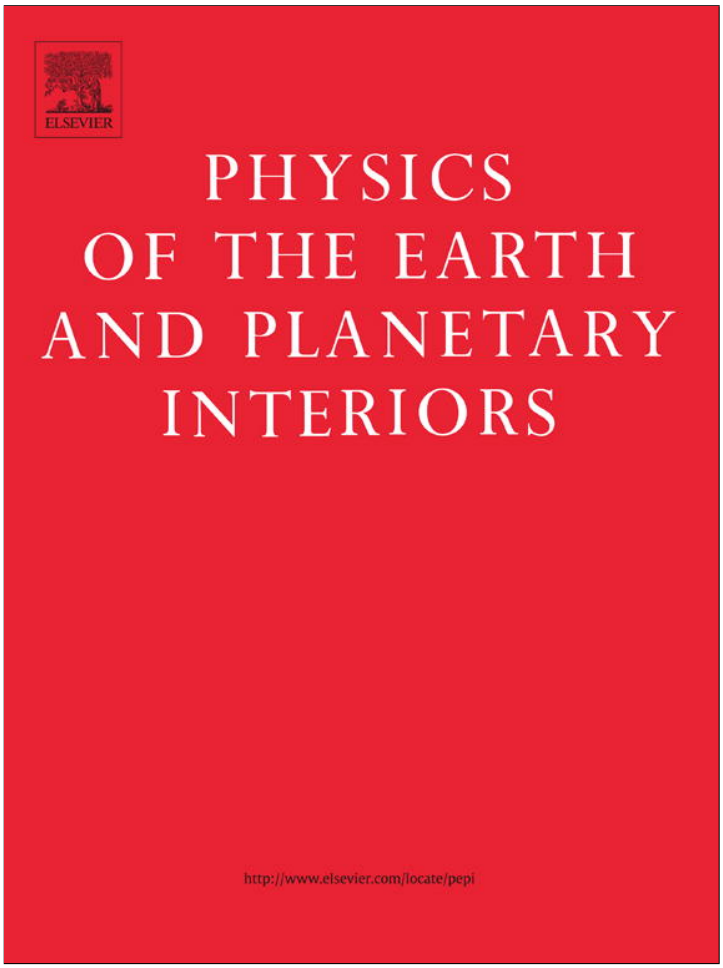


(This is a sample cover image for this issue. The actual cover is not yet available at this time.)

Physics of the Earth and Planetary Interiors 210-211 (2012) 36–49

Contents lists available at SciVerse ScienceDirect

Physics of the Earth and Planetary Interiors

journal homepage: www.elsevier.com/locate/pepi

# Assessing the uncertainties on seismic source parameters: Towards realistic error estimates for centroid-moment-tensor determinations

Andrew P. Valentine *, Jeannot Trampert

*Department of Earth Sciences, Universiteit Utrecht, P.O. Box 80021, 3508 TA Utrecht, The Netherlands*

ARTICLE INFO

*Article history:*
Received 13 March 2012
Received in revised form 6 June 2012
Accepted 20 August 2012
Available online 23 September 2012
Edited by George Helffrich

*Keywords:*
Seismic source
CMT algorithm
Source parameter uncertainty
Uncertainty estimation

ABSTRACT

The centroid-moment-tensor (CMT) algorithm provides a straightforward, rapid method for the determination of seismic source parameters from waveform data. As such, it has found widespread application, and catalogues of CMT solutions – particularly the catalogue maintained by the Global CMT Project – are routinely used by geoscientists. However, there have been few attempts to quantify the uncertainties associated with any given CMT determination: whilst catalogues typically quote a 'standard error' for each source parameter, these are generally accepted to significantly underestimate the true scale of uncertainty, as all systematic effects are ignored. This prevents users of source parameters from properly assessing possible impacts of this uncertainty upon their own analysis.

The CMT algorithm determines the best-fitting source parameters within a particular modelling framework, but any deficiencies in this framework may lead to systematic errors. As a result, the minimum-misfit source may not be equivalent to the 'true' source. We suggest a pragmatic solution to uncertainty assessment, based on accepting that any 'low-misfit' source may be a plausible model for a given event. The definition of 'low-misfit' should be based upon an assessment of the scale of potential systematic effects. We set out how this can be used to estimate the range of values that each parameter might take, by considering the curvature of the misfit function as minimised by the CMT algorithm. This approach is computationally efficient, with cost similar to that of performing an additional iteration during CMT inversion for each source parameter to be considered.

The source inversion process is sensitive to the various choices that must be made regarding dataset, earth model and inversion strategy, and for best results, uncertainty assessment should be performed using the same choices. Unfortunately, this information is rarely available when sources are obtained from catalogues. As already indicated by Valentine and Woodhouse (2010), researchers conducting comparisons between data and synthetic waveforms must ensure that their approach to forward-modelling is consistent with the source parameters used; in practice, this suggests that they should consider performing their own source inversions. However, it is possible to obtain rough estimates of uncertainty using only forward-modelling.



## 1. Introduction

The centroid-moment-tensor (CMT) algorithm, introduced by Dziewonski et al. (1981) and developed by Dziewonski and Woodhouse (1983a), has been extraordinarily successful. For 30 years, it has been routinely applied to seismic data, first under the auspices of the Harvard CMT Project, and latterly as the Global CMT Project.[1] The full catalogue – available from www.globalcmt.org – now contains details of over 35,000 earthquakes, and the information it contains has found wide application across the geosciences.

However, one important question has received relatively little attention over the years: what uncertainties should be assigned to the quoted source parameters? Knowledge of these uncertainties is necessary if catalogue event locations or moment tensors are to be used in the course of other studies: any errors in source parameters will propagate, and may affect results. For example, many global tomographic inversions rely on CMT parameters as part of their analysis (e.g. Panning and Romanowicz, 2006; Ritsema et al., 2011), which has been shown to risk introducing bias into the resulting models (Valentine and Woodhouse, 2010). Of course, a particular application may be insensitive to uncertainty-level changes in source parameters, or other sources of error may safely be assumed to dominate. However, such

* Corresponding author.
*E-mail address:* andrew@geo.uu.nl (A.P. Valentine).

[1] In this paper, we use the abbreviation 'CMT' to refer to the source determination algorithm *in general*, and not to any particular implementation. On occasion, we refer to the catalogue maintained by the Global CMT Project, as the best-known CMT-related resource; for the avoidance of doubt, we use the abbreviation 'GCMT' for this particular case. The reader should note that the authors of the present paper are not involved in maintaining the GCMT catalogue, and that there will be differences of detail between the GCMT approach, and ours.

0031-9201/$ - see front matter © 2012 Elsevier B.V. All rights reserved.
http://dx.doi.org/10.1016/j.pepi.2012.08.003

assessment can only be made if realistic CMT uncertainties are known.

The GCMT catalogue gives a 'standard error' in each parameter, derived from the inverse problem. However, this calculation assumes that uncorrelated data noise is the only source of error in the determination; systematic effects arising from incomplete knowledge of earth structure, or from the use of approximate methods for modelling wave propagation are ignored. Fig. 1 shows the distribution of errors in spatio-temporal coordinates for all events in the GCMT catalogue; we see that a typical event is said to have a location error of a few kilometres, and a time known to within a fraction of a second. Such values provide an important and useful measure of the stability of the CMT inversion for a given event, but are clearly rather optimistic if taken to denote our true state of knowledge about that earthquake. We stress that those responsible for curating the GCMT catalogue have never claimed otherwise (see, for example, Smith and Ekström, 1997; Ekström, 2011).

Experiments to test the robustness of the CMT algorithm have been reported by a number of authors, including Ferreira and Woodhouse (2006) and Hjörleifsdóttir and Ekström (2010), and others have compared CMT results with those obtained via fundamentally different means (e.g. Smith and Ekström, 1997; Helffrich, 1997; Kagan, 2003; Elliott et al., 2010; Weston et al., 2011). The detailed conclusions vary, but there is general agreement that spatial uncertainty should be measured in tens of kilometres, and times are known to within a few seconds. However, the methods used are typically computationally expensive, and not suited to routine determination of the errors specific to individual events.

In this paper, we examine how uncertainties may arise in the CMT determination process, and how these impact on the recovered source parameters. We begin by briefly summarising the CMT algorithm, and establishing a framework in which uncertainties may be estimated. We then attempt to illustrate and calibrate this framework using published source parameters and various inversion results for two recent events in the vicinity of New Zealand, although detailed results will require a case-by-case analysis. Finally, we demonstrate that similar results may be computed directly during CMT inversion, subject to the validity of a particular linear approximation.

## 2. The CMT algorithm: an overview

The CMT algorithm assumes that a seismic event can be modelled using ten parameters: the six independent components of the *moment tensor*, denoted $f_{1\ldots6}$; three spatial co-ordinates, $\vartheta_c$ (latitude), $\varphi_c$ (longitude) and $z_c$ (depth); and time, $t_c$. We therefore describe the source for a given event by a ten-component 'CMT vector',

$$\mathbf{m} = (f_1 \quad \cdots \quad f_6 \quad z_c \quad \vartheta_c \quad \varphi_c \quad t_c)^{\mathbf{T}}. \tag{1}$$

The background to this representation is developed in a number of papers (e.g. Backus and Mulcahy, 1976; Backus, 1977; Dziewonski and Woodhouse, 1983b), and is sketched in Appendix A; essentially, the approach involves the first-order terms in an expansion of the stress glut.

### 2.1. The source determination process

Given **m**, we have a variety of methods for the calculation of synthetic seismograms. Some, such as those based on numerical solution of the seismic wave equation (e.g. Komatitsch and Tromp, 2002a,b), have a high accuracy – and are correspondingly computationally expensive; others, such as most commonly-used formulations involving normal mode summation, rely on various approximations for the sake of efficiency (e.g. Woodhouse and Dziewonski, 1984; Romanowicz, 1988). All methods require knowledge of an earth model, and typically implementations will incorporate various other user-determined parameters and settings. Notwithstanding this, we can calculate synthetic seismograms, **s**, to correspond to some set of recordings of true ground motion represented by the data vector, **d**.

Real seismic data contains noise, and so we do not expect to be able to exactly reproduce **d**. Instead, we define a measure of the similarity of data and synthetic: the CMT algorithm adopts the least-squares waveform misfit

$$m^2(\mathbf{d},\mathbf{s}) = \frac{(\mathbf{d}-\mathbf{s})^{\mathbf{T}}(\mathbf{d}-\mathbf{s})}{\mathbf{d}^{\mathbf{T}}\mathbf{d}}. \tag{2}$$

This quantity is 0 if data and synthetic agree perfectly; a misfit greater than 1 implies that the residuals are larger than the original data. The 'best-fitting' synthetic seismograms to a given dataset are therefore those for which $m^2$ is minimal; typically, applications based on waveform-matching then assume that the noise component of **d** is sufficiently incoherent that the parameters used to generate **s** may be regarded as representative of the seismic event.

Thus, the CMT algorithm involves treating $m^2$ for a given dataset as a function of **m**, and finding the source parameters that give rise to the minimum misfit. We make the assumption that seismograms may be regarded as linearly dependent on **m**, so that

$$\mathbf{s}(\mathbf{m}+\Delta\mathbf{m}) = \mathbf{s}(\mathbf{m}) + \mathbf{A}\Delta\mathbf{m}, \tag{3}$$

where **A** is the matrix of partial derivatives

$$\mathbf{A} = \left(\frac{\partial\mathbf{s}}{\partial f_1} \quad \cdots \quad \frac{\partial\mathbf{s}}{\partial f_6} \quad \frac{\partial\mathbf{s}}{\partial z_c} \quad \frac{\partial\mathbf{s}}{\partial\vartheta_c} \quad \frac{\partial\mathbf{s}}{\partial\varphi_c} \quad \frac{\partial\mathbf{s}}{\partial t_c}\right). \tag{4}$$

Then, given some source vector $\mathbf{m_i}$, the well-known least-squares algorithm (see, for example, Menke, 1989) dictates that the minimum misfit solution is given by

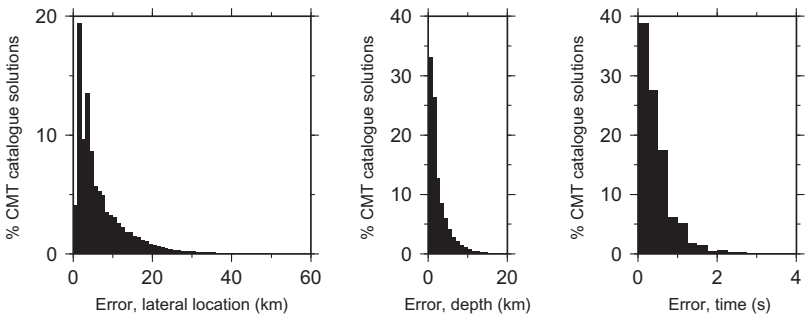


**Fig. 1.** Error distributions from GCMT catalogue. Histograms showing distribution of standard errors quoted by GCMT catalogue for lateral location (latitude and longitude, combined), depth (omitting events for which the depth parameter was reported as fixed to some *a priori* value), and time.

$$\mathbf{m_{i+1}} = \mathbf{m_i} + \left(\mathbf{A^T A}\right)^{-1}\mathbf{A^T}(\mathbf{d} - \mathbf{s}(\mathbf{m_i})). \quad (5)$$

If Eq. (3) were exactly true, it would be possible to exactly determine source parameters in a single step. Normal mode theory suggests that this is valid when the spatio-temporal co-ordinates of the centroid are held fixed: thus, an initial source $\mathbf{m_0}$ can be found by adopting hypocentral parameters derived from other measurements, such as found in the USGS 'Preliminary Determination of Epicenters' (PDE) catalogue (discussed in Sipkin et al., 2000). However, once these are allowed to vary, the problem becomes weakly non-linear, so that iteration with Eq. (5) is required. Typically, experience suggests that convergence is achieved with a few (5–10) iterations.

In practice, it is usually assumed that an indigenous source should have no explosive component, corresponding to a zero-trace constraint on the moment tensor (as defined in Appendix A, Eq. (A.12)). This implies that

$$f_1 + f_2 + f_3 = 0, \quad (6)$$

which may be incorporated into the least-squares algorithm via a Lagrange multiplier (e.g. Menke, 1989). Experience suggests that the algorithm will become unstable for very shallow events: these are therefore typically fixed to have $z_c = 15$ km. In certain circumstances, other components may also be fixed. It is possible to constrain the source so that it is a pure double-couple: this requires the determinant of the moment tensor to be zero. We do not apply this constraint in the current paper, although we plot the best-fitting double couple in addition to the non–double-couple source when showing focal mechanisms.

### 2.2. Data

In principle, the CMT algorithm may be applied to any class of waveform data, provided that methods exist for the calculation of synthetics and the appropriate partial derivatives. Typically, CMT determinations are performed using long-period teleseismic data, drawn from major international seismic networks: for best results, a good azimuthal distribution of stations is required. The GCMT catalogue makes use of up to three data types (see, for example, Hjörleifsdóttir and Ekström, 2010; Ekström et al., 2012): 'body waves', the portion of the seismogram before the main surface wave arrival, filtered to have a dominant period at around 50 s; 'surface waves', with a similar frequency content but windowed to capture the main surface wave-train; and 'mantle waves', longer-period (dominant period around 135 s) surface waves. As we shall see, each class of data has its own characteristics and sensitivities, and in practice the source parameters indicated by each may differ.

## 3. Uncertainty and the CMT algorithm

From this brief outline, it should be clear that the CMT algorithm relies on a number of assumptions, and that these have the potential to impact the recovered source parameters. In particular, any inaccuracies in earth model or wave propagation framework may generate waveform errors in the synthetic seismograms, introducing systematic biases into results. However, in order to ascribe an 'uncertainty' to each parameter, we must recognise that at least two distinct uses for source parameters exist, and that these groups of users may have somewhat different expectations.

### 3.1. Source parameters for wave propagation

The first main use for seismic source parameters is to allow waveform modelling (for example, in order to perform tomographic inversion). Typically, such users are primarily interested in the accuracy of the waveforms produced, rather than in the source parameters themselves. By definition, the CMT algorithm yields the source that allows a given choice of earth model and wave propagation framework to best explain some dataset. For self-consistency, forward-modelling must be performed using the same choices as were made during source determination. If this is the case, and the user is prepared to regard the chosen modelling framework and earth model as correct, uncertainty in the source parameters arises only from the presence of noise within the data. For these users, catalogue standard errors may provide reasonable estimates of uncertainty.

In order to understand how these errors are calculated, we must adopt a more sophisticated formulation of the least-squares algorithm than that set out in Eq. (5). If we assume that the uncertainty distributions associated with data and model parameters are Gaussian, this may be rewritten in the form (e.g. Tarantola, 1987; Mosegaard and Tarantola, 2002)

$$\mathbf{m_{i+1}} = \mathbf{m_i} + \left(\mathbf{A^T C_D^{-1} A} + \mathbf{C_M^{-1}}\right)^{-1}\mathbf{A^T C_D^{-1}}[\mathbf{d} - \mathbf{s}(\mathbf{m_i})] + \mathbf{C_M^{-1}}(\mathbf{m_i} - \mathbf{m}_{\text{prior}}), \quad (7)$$

where $\mathbf{C_D}$ and $\mathbf{C_M}$ are the *a priori* data and model covariance matrices, respectively, and $\mathbf{m}_{\text{prior}}$ represents our *a priori* model. The *a posteriori* model covariance, which describes the uncertainties on the resulting model parameters, can then be estimated as

$$\widetilde{\mathbf{C}}_\mathbf{M} = \left(\mathbf{A^T C_D^{-1} A} + \mathbf{C_M^{-1}}\right)^{-1}. \quad (8)$$

The CMT algorithm does not make use of any damping during matrix inversion, so that $\mathbf{C_M^{-1}} = \mathbf{0}$. This corresponds to the assertion that *a priori* constraints on model parameters are 'infinitely weak' (Tarantola and Valette, 1982). If we then make the assumption that all data are independent, with uncertainty characterised by a Gaussian of width $\sigma$, we have $\mathbf{C_D} = \sigma^2\mathbf{I}$; $\sigma$ can be derived from the misfit between data and synthetic, by regarding the numerator as a sum of samples from the Gaussian. Thus, we obtain $\widetilde{\mathbf{C}}_\mathbf{M} = \sigma^2\left(\mathbf{A^T A}\right)^{-1}$, and the diagonal terms of this matrix may be interpreted as the 'standard errors' on the model parameters.

In formulating the problem in this manner, we are assuming that all errors are Gaussian, and independent. Both these assumptions are almost certainly incorrect; in particular, correlations are likely to exist between the uncertainties at different points in the time series, and perhaps between those observed at different stations. Within the Gaussian framework, such correlations would result in a non-diagonal data covariance matrix, $\mathbf{C_D}$, and could alter our interpretation of the resulting uncertainties on model parameters (e.g. Langbein and Johnson, 1997). Of particular interest for the current case is the work of Yagi and Fukahata (2008, 2011), who attempt to incorporate a more realistic data covariance matrix during inversion for earthquake slip distribution – note that a non-diagonal $\mathbf{C_D}$ in Eq. (7) could affect the solution itself, as well as the uncertainties related to it. However, estimating the structure of the covariance matrix is not straightforward; typically, various stochastic models are used (e.g. Lohmann and Simons, 2005). Nevertheless, the effects are likely to be relatively small compared to those attributable to inaccuracies in earth model or wave propagation framework. As a result, and in common with mainstream implementations of the CMT algorithm, we therefore persist with the assumption of independent errors.

Unfortunately, standard error analysis breaks down as soon as unmodelled effects are present in the data. To illustrate this, Fig. 2 demonstrates a toy problem, where we attempt to locate the minimum of a function given only noisy samples from it. We choose (incorrectly) to model the function as quadratic; the best-fitting coefficients can be found, along with the standard Gaussian

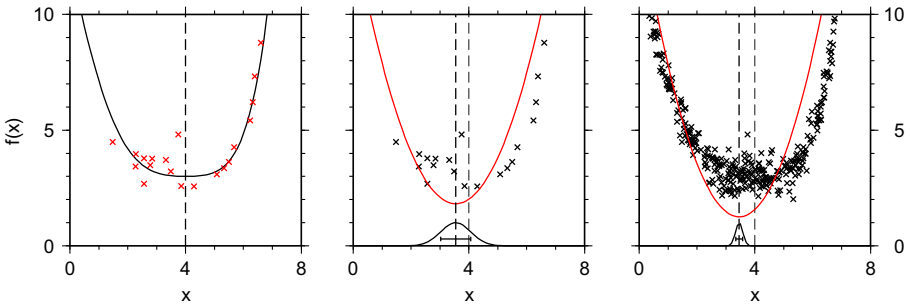


**Fig. 2.** Over-confidence in the model leads to over-confidence in results. We wish to find the value of $x$ that minimises $f(x)$, given noisy samples from $f(x)$ (left panel). If we assume (wrongly) that $f(x)$ is a quadratic, the least-squares algorithm allows us to find the best-fitting solution, and we can estimate the error in the location of $x_{\min}$ (centre panel) – as indicated by the error bar and (unnormalised) corresponding Gaussian distribution. Increasing the number of samples increases our confidence in this location (right panel), so that the 'true' location of the minimum no longer lies within the region permitted by uncertainty analysis.

errors in these. It is then straightforward to locate the minimum of the function, and use the rules governing uncertainty propagation (e.g. Squires, 2001) to compute the error-bars on this location. When relatively few data points are available, results are reasonable – the correct value lies within the calculated error. However, as more data are used, the location of the best-fitting quadratic becomes increasingly tightly constrained, and our analysis indicates an incorrect location with a high degree of confidence. This arises because we are failing to take discrepancies between model and reality – systematic errors – into account during error analysis.

The source parameters that yield the best fit between data and synthetics for one choice of earth model and modelling framework need not be optimal when different choices are made. In fact, as we shall see, changing from one 'reasonable' setup to another can have a serious effect on waveform misfit – in particular, the definition of misfit in Eq. (2) is very sensitive to changes that induce phase shifts in the synthetic seismograms. Ignoring this fact has the potential to generate misleading results when synthetic seismograms are used – see, for example, Valentine and Woodhouse (2010). Unfortunately, complete information about the setup used for calculation of catalogue source parameters is rarely available – and it is rarer still for this setup to coincide with the setup a particular user wishes to adopt. One solution may be for researchers to consider performing their own source inversions, so that self-consistency can be ensured. Failing this, we believe the uncertainty on source parameters must be assessed in terms of geological accuracy.

### 3.2. Geologically accurate source parameters

For many users, geological accuracy is important. For any seismic event, a correct centroid location and moment tensor exist, and these users regard the output from the CMT algorithm as an estimate of this. Estimating the geological uncertainty is a much more complex problem: a full treatment would require an understanding of the uncertainties associated with current earth models and wave propagation techniques, in addition to a proper analysis of the noise in seismic data. However, it is possible to develop reasonable estimates from an assessment of the impact these uncertainties are likely to have on waveform misfit.

One advantage to adopting this definition of source parameter uncertainty is that – for at least some events – it is possible to compare CMT results with those derived by other methods, and with field observations. However, caution must be exercised: other methods will have their own uncertainties, and these may be equally poorly-understood. It is also important to recognise that the spatio-temporal centroid location for a seismic event may not correspond well to natural physical observables: for example, events on a fault that is not straight may have centroid locations that do not lie on the fault. Obviously, a ten-parameter source description represents a hugely simplified model for the complexities of earthquake faulting processes, and this must also be considered during analysis: for discussion of alternative source models, see Madriaga (2007).

Even the best-available earth models and forward modelling techniques do not faithfully match the behaviour of the real Earth. Moreover, for reasons of computational efficiency and historical continuity, routine determinations are typically performed using low-resolution models, and approximate forward modelling, although some studies have made use of fully-numerical techniques (e.g. Liu et al., 2004). For example, according to Ekström et al. (2005) and Hjörleifsdóttir and Ekström (2010), determinations for the GCMT catalogue currently rely on normal mode summation with lateral heterogeneity incorporated through the path average approximation (Woodhouse and Dziewonski, 1984); some calculations are performed in a spherically-symmetric model (PREM; Dziewonski and Anderson, 1981), whilst others make use of the degree-8 model SH8/U4L8 (Dziewonski and Woodward, 1992; Dziewonski et al., 1992), with attenuation corrections derived from Durek and Ekström (1996). Thus, the best-fitting source in a given model is unlikely to be identical to the optimal source in the real Earth. However, provided that the model used is reasonable, the geologically-correct source should yield a *low* misfit.

We therefore propose a pragmatic approach to estimating the range of source parameters plausible for a given event. We define a misfit threshold,

$$m^2_{\text{thresh}} = (1+\phi)m^2_{\min}, \tag{9}$$

where $m^2_{\min}$ is the minimum misfit found by application of the CMT algorithm, and $\phi$ is some small positive number. We then assert that any source generating misfit $m^2 \leqslant m^2_{\text{thresh}}$ is to be regarded as a plausible model for the event; the set of all such sources defines our uncertainties around the best-fitting parameters. Of course, this strategy is not a proper statistical treatment of errors, and it relies on a more-or-less *ad hoc* choice of value for $\phi$. However, we hope that it will prove sufficient for practical purposes.

To make use of this, we must develop some method for mapping out the appropriate region of source parameter-space. One route lies in 'most-squares inversion' (Jackson, 1976; Meju and Hutton, 1992), which seeks to find extremal values of parameters subject to an overall constraint on misfit. However, this requires a computationally expensive inversion process for any choice of $\phi$, and does not provide any immediate sense of the tradeoff between $\phi$ and the resulting uncertainty estimates. A simpler approach, and the one that we shall follow, lies in mapping out the misfit function through forward modelling. This has the additional benefit of requiring only readily-available tools for computing synthetic seismograms, making it accessible to users who may wish to explore the extent to which particular source parameters are

constrained without necessarily having the software or expertise necessary to perform source determinations. However, our previous argument regarding self-consistency still applies: caution should be exercised when using catalogue parameters in conjunction with different datasets and modelling approaches.

## 4. Forward modelling and the misfit function

To illustrate our approach, we assess the extent to which the CMT algorithm can constrain the source parameters for the earthquake that struck Darfield, near Christchurch, New Zealand at 16:35 on 3 September 2010 (UTC). This event has been studied by a number of different groups, using a variety of methods and datasets.

### 4.1. High-quality synthetic seismograms

In order to avoid complications due to noise, and so that 'correct' source parameters are known, we conduct our analysis using synthetic seismograms. We adopt the GCMT catalogue source parameters for this event, as set out in Table 4, and make use of the degree-40 earth model, S40RTS (Ritsema et al., 2011) in conjunction with fully-numerical wave propagation (SPECFEM3D_GLOBE v.5.1.1, Komatitsch and Tromp, 2002a,b; Komatitsch et al., 2010). We use a global station distribution, based on the IRIS/IDA and IRIS/USGS networks (network codes II and IU), restricted to epicentral distances in the range $40^\circ \leqslant \theta_E \leqslant 140^\circ$, as shown in Fig. 3, and compute three hours of three-component data for each, beginning at the event time. The resulting seismograms are convolved with a triangular source time function, of half-width 10 s, and then up to three frequency-time windows are extracted from each trace. These windows conform to the definitions given in Table 1, and are designed to contain particular classes of data. We refer to these filtered waveforms as the 'high-quality synthetic dataset', for which the 'true source' is the GCMT source.

### 4.2. Approximate synthetic seismograms

Using the same set of source parameters, but the degree-8 model M84C (Woodhouse and Dziewonski, 1984) and normal mode summation under the path-average approximation, we compute a second, equivalent, set of synthetic seismograms. Again, we convolve the output from our calculations with a triangular source time function of half-width 10 s, and perform identical windowing operations. We refer to the result as the 'approximate synthetic dataset'; any differences between this and the high-quality dataset are attributable to changes in earth model and forward-modelling strategy. We suggest that these differences are of a similar scale and character to those that might be expected between the real Earth, and the approximate synthetic seismograms typically utilised for CMT inversion.

To illustrate these differences, we compute the waveform misfit (Eq. (2)) between high-quality and approximate datasets, on a window-by-window basis. These are plotted in Fig. 3. The different modelling approaches do not affect all window types equally: typically, best fit is seen with mantle waves, and surface waves agree least well. It is unsurprising that we see better agreement with long-period data: these will be less sensitive to the short-wavelength structure that is absent from M84C. Regional effects can be observed, based on the overall differences in character of the earth models used – for example, the waveform agreement observed using body wave windows is notably worse in North America than in other parts of the world.

From this, it should be apparent that inconsistencies in modelling approach can lead to quite different waveforms, and this reinforces the need for self-consistency when source parameters are used. In addition, these differences arise in a complex manner, affecting particular regions and frequency bands in different ways. We therefore anticipate that each data type will behave differently during CMT inversion, and that a solution based on a combination of all three will be some compromise between the individual behaviours.

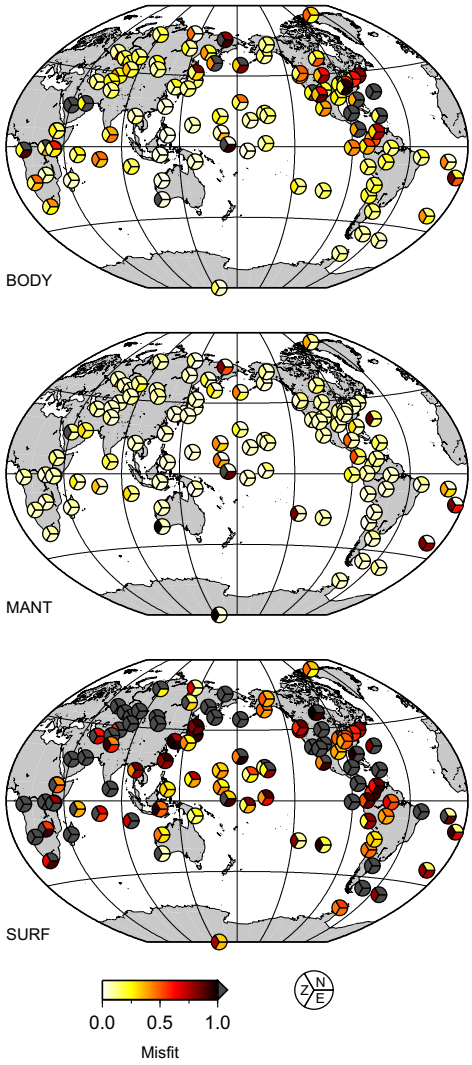


**Fig. 3.** Waveform deficiencies in approximate dataset. Misfit between seismograms in high-quality synthetic dataset, and their counterparts in the approximate dataset, computed according to Eq. (2). Each trace contributes up to three windows, according to the definitions set out in Table 1; we show each separately. Stations with a misfit value greater than 1 are shown in grey; such misfit values imply that the 'error' inherent in the approximate synthetic is greater than the true trace.

**Table 1**
Definitions of windows used in modelling. Each window is defined relative to seismic phase arrivals (P:P-wave; $R1/R2$: first and second surface wave trains), and is only used if it meets a minimum length criterion. Phase arrival times are computed using PREM (Dziewonski and Anderson, 1981; Crotwell et al., 1999). Each window is cosine band-pass filtered, with pass-band defined by the periods $T_{1,\ldots,4}$.

| Name | Window | | | Filter | | | |
|---|---|---|---|---|---|---|---|
| | Start | End | Min | $T_1$ | $T_2$ | $T_3$ | $T_4$ |
| BODY | $P-300$ s | $R1-300$ s | 300 | 1000 | 500 | 60 | 45 |
| MANT | $P-300$ s | $R2+1800$ s | 1800 | 1000 | 500 | 150 | 135 |
| SURF | $R1-600$ s | $R2+600$ s | 1800 | 1000 | 500 | 60 | 45 |

### 4.3. Mapping out the misfit function

In order to understand the degree of constraint the misfit function (Eq. (2)) provides on source parameters, we must map out $m^2(\mathbf{m})$. To do this in an efficient manner, we adopt an approach based on random sampling, and generate 10,000 sets of source parameters that are 'close' to the true source. The algorithm we use to do this is straightforward, and is set out in Appendix B. For each of these random sources, we compute and process synthetic seismograms as before, using M84C and normal mode summation. We compare these to the high-quality synthetic dataset, and thus obtain 10,000 samples from the misfit function for each of the three data types defined in Table 1. We plot all samples for which $m^2 \leqslant 1$ in Figs. 4–6. We note that 10,000 samples represents a low sampling density in nine-dimensional space (not ten-dimensional, as our sampling strategy preserves the zero-trace constraint), but for current purposes we believe it to be sufficient: the misfit function is known to be smooth and relatively slowly-varying, and we are not attempting a *Monte Carlo*-style analysis, for which a proper sampling density is imperative.

From Figs. 4–6, a number of observations can be made:

1. For body and surface wave datasets, sources can be found that explain the 'data' (the high-quality synthetic dataset) much

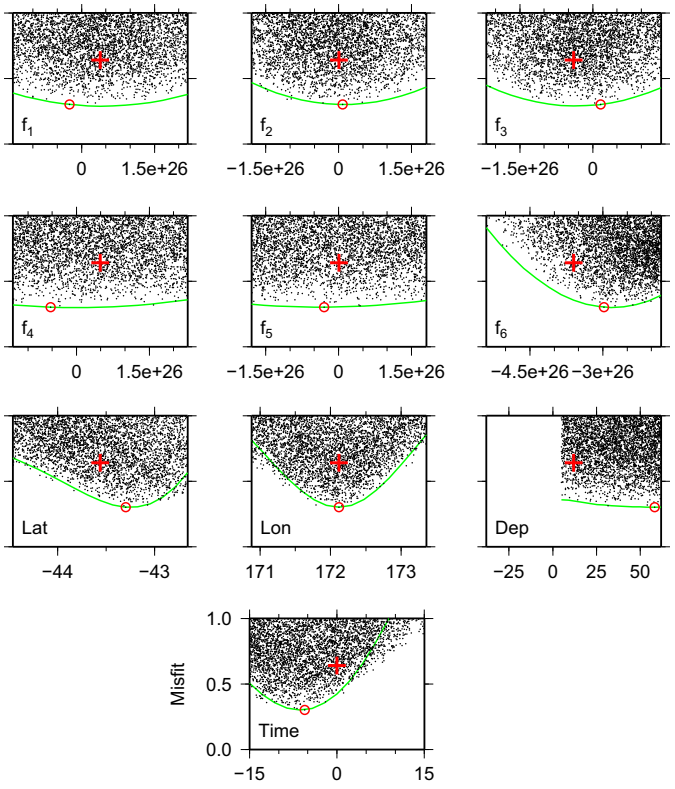


**Fig. 4.** The misfit function, as seen by body waves. A single, high-quality synthetic dataset was generated for a known ('true') source; then, 10,000 sets of approximate synthetic seismograms were computed for source parameters distributed at random about the true source. For each source, we extract body waves according to the definition in Table 1, and compute the misfit (Eq. (2)) between high-quality and approximate datasets. We show misfit as a function of source parameter for all examples with $m^2 \leqslant 1$; every sample shown appears in each of the ten plots. The misfit obtained when approximate synthetics are computed using the true source is denoted by a red cross; the sample yielding the lowest misfit is circled. Green lines provide an estimated lower bound to the samples, computed by varying each source parameter in turn from the optimal sample; for full details, see text. Equivalent plots for mantle- and surface-wave data are shown in Figs. 5 and 6, respectively. (For interpretation of the references to colour in this figure legend, the reader is referred to the web version of this article.)

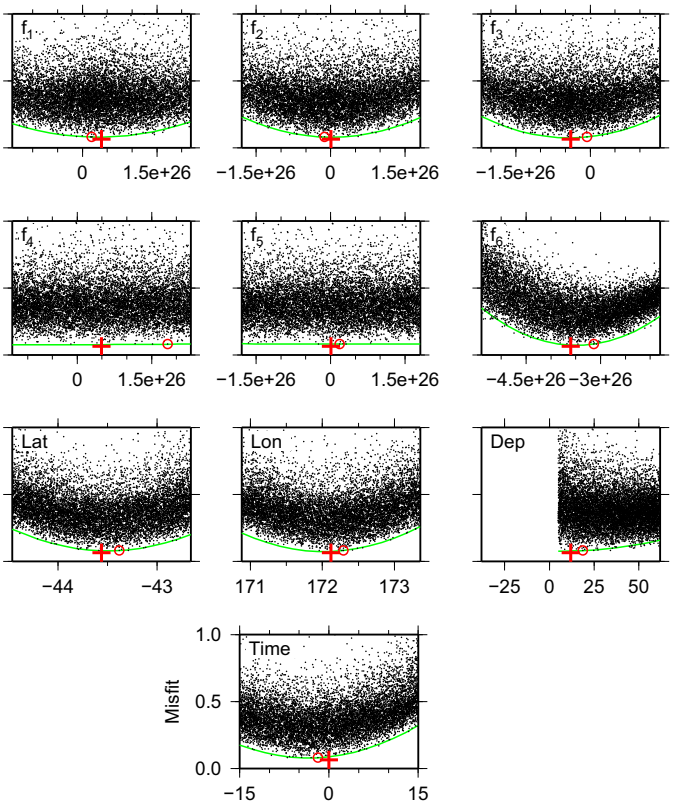


**Fig. 5.** The misfit function, as seen by mantle waves. See Fig. 4 for full explanation.

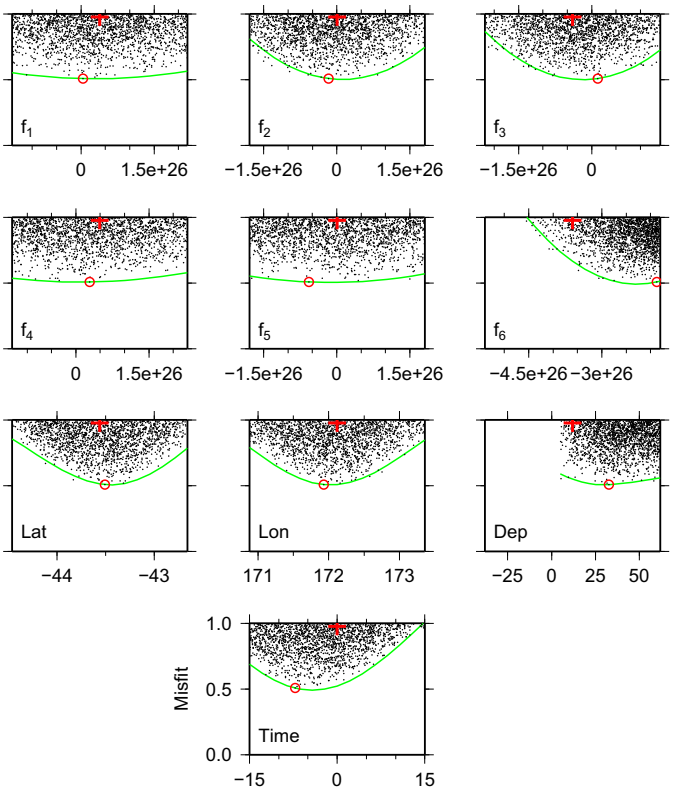


**Fig. 6.** The misfit function, as seen by surface waves. See Fig. 4 for full explanation.

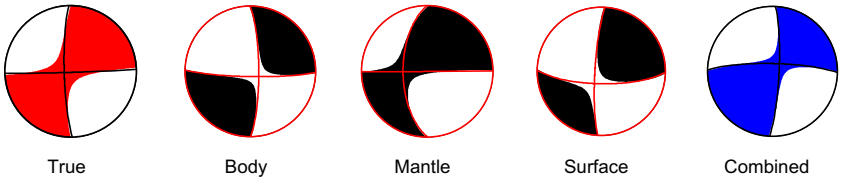


**Fig. 7.** Best-fitting random moment tensor for each data type. From left to right: the 'true' moment tensor, used in calculating high-quality synthetic data; best-fitting example generated by random sampling for body, mantle and surface wave data types (i.e. circled sources from Figs. 4–6); best-fitting example generated by random sampling when all three data types are combined. Best-fitting double-couple solution is overlain in each case.

better than the true source, indicated by a red cross in each plot. In general, these represent relatively modest differences in true and best-fitting parameters, although there are some notable discrepancies – particularly the behaviours of $f_6$, depth and time. These differences lie at the heart of the 'biasing' effect described by Valentine and Woodhouse (2010): errors in the earth model are partly accommodated via shifts in source parameters.

2. As in Fig. 3, there are differences in behaviour between the various data types. Minima fall at different parameter values, and the curvature of the misfit surface varies – note that all figures share a common scale. The focal mechanism corresponding to the best-fitting random example in each case is shown in Fig. 7. From these, it appears that the differences have relatively minor effects on the overall character of the recovered source, although some differences may be seen.
3. Not all parameters are well-constrained by all data types. This is particularly true for components $f_4$ and $f_5$, which are well-known to be difficult to resolve for shallow sources (e.g. Dziewonski et al., 1981); however, other components fare little better.

Typically, we wish to combine all available data to arrive at a single source determination. This is done by forming a single misfit function,

$$m^2 = \frac{\sum_\lambda w_\lambda (\mathbf{d}_\lambda - \mathbf{s}_\lambda)^{\mathbf{T}} (\mathbf{d}_\lambda - \mathbf{s}_\lambda)}{\sum_\lambda w_\lambda \mathbf{d}_\lambda^{\mathbf{T}} \mathbf{d}_\lambda} = \frac{\sum_\lambda w_\lambda \mathbf{d}_\lambda^{\mathbf{T}} \mathbf{d}_\lambda m_\lambda^2}{\sum_\lambda w_\lambda \mathbf{d}_\lambda^{\mathbf{T}} \mathbf{d}_\lambda}, \tag{10}$$

where the index $\lambda$ is used to refer to the various data types used, and $w_\lambda$ is a weight assigned to each. Thus, the overall misfit curve is essentially a weighted average of the individual misfit curves, and the location of the minimum is governed by the relative weights. Various approaches to weighting are possible, and detailed results will depend on the one adopted. For the purposes of this paper, we choose $w_\lambda = 1/\mathbf{d}_\lambda^{\mathbf{T}} \mathbf{d}_\lambda$, which leads to a particularly straightforward combination in Eq. (10), so that each dataset contributes equally to the overall calculation.

The misfit distributions produced by combining our datasets in this manner are shown in Fig. 8, with the focal mechanism for the best-fitting of the random sources given in Fig. 7. As expected, the behaviour mirrors that for the individual data types, and generally parameters are reasonably close to the true values. However, where body and surface wave data show significant errors, this is reflected in the combined results.

### 4.4. Estimating uncertainties

As discussed above, our proposed approach to uncertainty assessment involves determining the range of sources that yield misfit below some threshold. In order to calculate this efficiently, we require a method for estimating the curve describing the lower bound of the distributions shown in Figs. 4–6 and 8. This may be achieved by systematically varying each source parameter in turn away from the minimum-misfit solution, computing synthetic

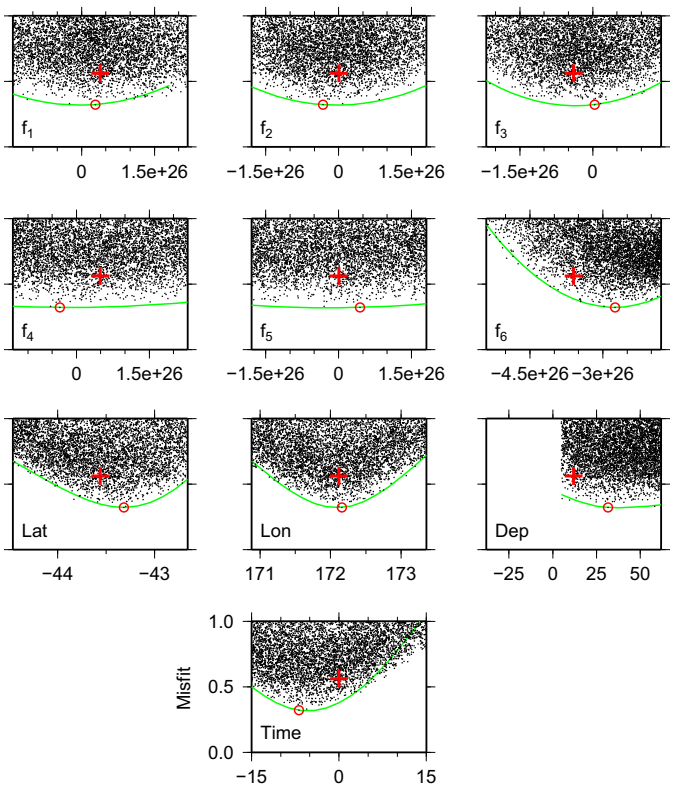


**Fig. 8.** The misfit function, all three data types combined. Each data set was weighted so that $\mathbf{d}^{\mathbf{T}}\mathbf{d}$ is equivalent; other choices of weighting scheme are equally possible. See Fig. 4 for explanation.

seismograms, and calculating the resulting misfit. For most accurate results, we should perform a constrained inversion to select the source parameters to use in each case: the value for one parameter is chosen *a priori*, and then the remaining nine are chosen to yield the lowest misfit possible. However, this is a computationally-intensive procedure, since numerous samples are required for each curve.

Since the dependence of seismograms on source parameters is approximately linear – at least close to the minimum-misfit solution – adequate results may be obtained through forward-modelling alone, fixing all source parameters to the minimum-misfit values, except the parameter explicitly varying. The green curves in Figs. 4–6 have been produced in this manner based on the best-fitting random source (as circled): 15 equally-spaced measurements of misfit define each curve. The best-fitting random source is close to the minimum-misfit source that would be obtained by the CMT inversion, and this could also be used as a starting-point for calculating the curves. When obtaining curves for components $f_{1\ldots3}$, we enforce the zero-trace constraint (Eq. (6)) by adjusting the two 'non-varying' parameters in proportion to their original magnitudes. The resulting curves do not exactly

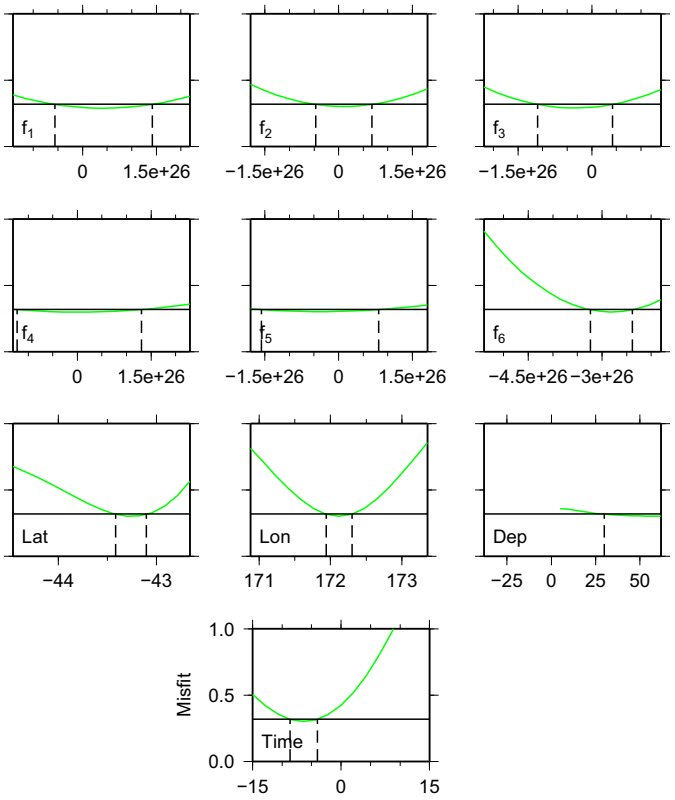


**Fig. 9.** A range of source parameters are compatible with a 'low-misfit' solution. Green curves are identical to those in Fig. 4, and represent the lower bounds of the misfit distributions observed with body wave data. The best-fitting random source yielded $m^2 = 0.289$; horizontal line signifies this plus 10%. This allows us to identify a range of source parameters yielding a good – though not optimal – fit to our high-quality synthetic data; see Table 2 for numerical values. Plots for other data types are similar, and are omitted for brevity. (For interpretation of the references to colour in this figure legend, the reader is referred to the web version of this article.)

bound the distributions found by random sampling, sometimes slightly over-estimating the misfit for parameters far from the best-fitting solution. However, these effects are unlikely to be significant in the context of our *ad hoc* treatment of uncertainty. In any case, researchers are more likely to have ready access to forward-modelling tools than the machinery for performing source inversions: subject to the need for self-consistency that has already been discussed, this approach may allow users to develop a sense for the degree to which the catalogue source parameters for a particular event may be constrained.

Using these curves, it is straightforward to estimate parameter ranges corresponding to any choice of $\phi$ in Eq. (9). For illustrative purposes, we adopt $\phi = 0.1$, representing a misfit threshold 10% greater the best obtainable; Fig. 9 shows this applied to the body wave dataset. Ranges indicated by each of the three datasets separately, and combined, are listed in Table 2; we note that the 10% threshold is sufficient for the range to encompass the 'true' value of most source parameters. However, it should be remembered that these ranges represent extremal values, where only one parameter is contributing to misfit change, and in practice, waveform errors are likely to impact on all ten source parameters. Thus, typical uncertainties may be rather lower; in any case, the choice of a 10% threshold is *ad hoc*, and as we shall see, may be rather pessimistic.

## 5. Application to real data

So far, we have conducted synthetic experiments only. Whilst these have the advantage of providing a known 'true' solution, they lack many of the complications of real data – such as noise, or realistic rupture models. We therefore obtain seismic waveforms for the Darfield event, again using the IRIS/IDA and IRIS/USGS networks. As before, these are windowed automatically for body, surface and mantle waves; the automatic windows are then adjusted by hand to correct for un-modelled effects and to remove poor-quality traces. We then perform five iterations of inversion according to the CMT algorithm, as described Section 2. For consistency with our synthetic experiments, we adopt $w_\lambda = 1/\mathbf{d}_\lambda^{\mathbf{T}}\mathbf{d}_\lambda$ and use the earth model M84C.

After five iterations, we find the misfit between data and synthetic to be essentially static: further iterations lead to no significant changes. The best-fitting solution is given in Table 3, with the focal mechanism shown in Fig. 10. The misfit obtained is 0.466, which we consider to be reasonably good for a real data inversion. Using this source, we then estimate the curves corresponding to the bottom of the misfit distribution, as described above, and identify the ranges of source parameters indicated by misfit thresholds of 1%, 5% and 10%. The resulting upper and lower bounds are also given in Table 3, with the corresponding focal mechanisms shown in Fig. 11. Whilst the numerical values admissible for each source parameter encompass a moderate range, Fig. 11 demonstrates that the overall character of the source remains reasonably well-constrained. We note that although the

**Table 2**
Range of source parameters within 10% of minimum misfit, synthetic experiment. As illustrated in Fig. 9, we estimate the range of values that are permissible for each source parameter subject to the constraint that misfit should not increase by more than 10% from the 'optimal' value (given in table as 'best fit'), for each of the three data types. In each case we quote upper and lower bounds; '–' indicates that no bound was found within the range of values in our experiment. Moment tensor components $f_{1,\ldots,6}$ are given in units of $10^{26}$ dyn cm, latitude and longitude in degrees, and depth in kilometres. Time is quoted as a shift in seconds relative to the 'true' source time used for computing the high-quality synthetic data. This 'true' source is given for reference.

| | | Body | | Mantle | | Surface | | Combined | |
|---|---|---|---|---|---|---|---|---|---|
| | 'True' | Min | Max | Min | Max | Min | Max | Min | Max |
| $f_1$ | 0.385 | −0.558 | 1.420 | −0.165 | 0.799 | – | 2.056 | −0.883 | 0.997 |
| $f_2$ | 0.008 | −0.466 | 0.675 | −0.384 | 0.437 | −0.695 | 0.917 | −0.897 | 0.842 |
| $f_3$ | −0.392 | −1.102 | 1.302 | −0.930 | 0.100 | −0.970 | 0.630 | −1.189 | 0.463 |
| $f_4$ | 0.491 | −1.228 | 1.302 | – | – | – | 1.923 | – | 2.001 |
| $f_5$ | 0.010 | −1.573 | 0.816 | – | – | – | 1.627 | – | – |
| $f_6$ | −3.600 | −3.238 | −2.379 | −3.942 | −3.030 | −3.097 | – | −3.338 | −2.193 |
| Lat | −43.56 | −43.41 | −43.10 | −43.72 | −43.27 | −43.77 | −43.13 | −43.59 | −43.08 |
| Lon | 172.12 | 171.84 | 172.30 | 171.66 | 172.39 | 171.58 | 172.49 | 171.77 | 172.40 |
| Dep | 12.0 | 29.84 | – | – | 28.73 | 10.38 | 61.02 | 18.54 | – |
| Time | 0.0 | −8.6 | −4.0 | −6.9 | 0.1 | −10.3 | 1.9 | −9.34 | −1.34 |
| $m^2_{\text{min}}$ | | 0.289 | | 0.080 | | 0.507 | | 0.321 | |
| $m^2_{\text{thresh}}$ | | 0.318 | | 0.088 | | 0.558 | | 0.353 | |

**Table 3**
Results, inversion of real data. Waveforms from the 3rd September 2010 Darfield earthquake are inverted using the CMT algorithm and earth model M84C (Woodhouse and Dziewonski, 1984), leading to source denoted 'Best'. Ranges of source parameters corresponding to misfit thresholds 1%, 5% and 10% above the best-fitting value are also quoted, according to the method set out in this paper. For comparison, we also perform inversion of the same dataset using earth model PREM (Dziewonski and Anderson, 1981) without any lateral heterogeneity, and the 3D model S20RTS (Ritsema et al., 2004). All moment tensor components are stated in units of $10^{26}$ dyne cm; latitude and longitude are given in degrees, depth in kilometres and time in seconds relative to the GCMT centroid time, 16:35:57.9 UTC.The focal mechanisms corresponding to the data in this table can be seen in Figs. 10 and 11.

| | | 1% Threshold | | 5% Threshold | | 10% Threshold | | | |
|---|---|---|---|---|---|---|---|---|---|
| | Best | Min | Max | Min | Max | Min | Max | PREM | S20RTS |
| $f_1$ | 0.615 | 0.327 | 0.915 | −0.059 | 1.286 | −0.347 | 1.572 | 0.685 | 0.551 |
| $f_2$ | −0.163 | −0.528 | 0.190 | −0.988 | 0.656 | −1.331 | 1.006 | −0.201 | 0.030 |
| $f_3$ | −0.451 | −0.726 | −0.162 | −1.110 | 0.205 | −1.391 | 0.484 | −0.483 | −0.581 |
| $f_4$ | −0.436 | −1.381 | 0.512 | −2.555 | 1.680 | −3.432 | 2.561 | −0.619 | −0.049 |
| $f_5$ | −0.502 | −1.333 | 0.330 | −2.368 | 1.365 | −3.142 | 2.140 | −0.716 | −0.267 |
| $f_6$ | −3.008 | −3.280 | −2.740 | −3.655 | −2.359 | −3.927 | −2.084 | −3.216 | −2.853 |
| Lat | −43.61 | −43.73 | −43.50 | −43.90 | −43.34 | −44.03 | −43.22 | −43.54 | −43.42 |
| Lon | 172.15 | 172.02 | 172.30 | 171.80 | 172.51 | 171.64 | 172.67 | 172.22 | 172.46 |
| Dep | 29.38 | 24.55 | 34.64 | 17.92 | 42.55 | 13.29 | 49.25 | 19.92 | 35.78 |
| Time | 2.0 | 0.5 | 3.8 | −2.1 | 6.0 | −3.8 | 7.8 | −2.3 | 1.1 |
| $m^2_{\min}$ | 0.466 | | | | | | | 0.454 | 0.489 |

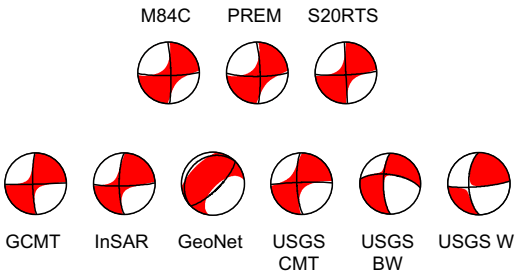


**Fig. 10.** Focal mechanisms for Tables 3 and 4. 'Beachballs' corresponding to sources recovered by inversion of real data in three different models (top row), and by other groups using a variety of data sources and methods (bottom row). Best-fitting double couples are overlain in black.

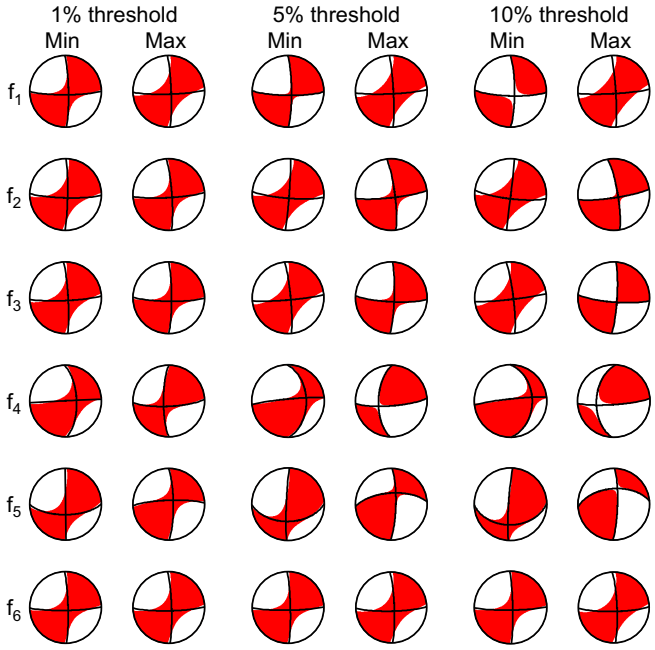


**Fig. 11.** Focal mechanisms corresponding to misfit thresholds. 'Beachballs' corresponding to the sources yielding upper and lower bounds for each parameter according to misfit thresholds of 1%, 5% and 10%, as set out in Table 3. Best-fitting double couple is overlaid in black for each mechanism.

best-fitting source has some non–double-couple component, it is possible to find sources within the 1% threshold that have an almost pure double-couple form (see, e.g. Julian et al., 1998; Miller et al., 1998).

### 5.1. Comparison with other determinations

For comparative purposes, we also perform source inversions using identical dataset and modelling choices, except for the earth model: we use both PREM without any lateral heterogeneity (Dziewonski and Anderson, 1981), and the degree-20 3D model S20RTS (Ritsema et al., 2004). The resulting source parameters are given in Table 3, with focal mechanisms depicted in Fig. 10. Again, differences in the character of the source are relatively minor, although typical changes in numerical values may be of the order of 10–20%. Whilst these effects may seem insignificant for the purpose of identifying the event mechanism, they may be important where waveform modelling is attempted: the seismogram calculated for a particular station may change markedly. Spatio-temporal changes between earth models may also be notable; we shall return to this shortly.

The Darfield earthquake has been studied by a number of researchers, using a variety of datasets and techniques. As a result, numerous moment tensors are available in published literature and databases, and a few are presented in Table 4 and Fig. 10. In addition to the GCMT solution, already encountered in the context of computing synthetic datasets, we show the USGS CMT solution, obtained using an implementation of the CMT algorithm intended to yield reliable automatic results for large earthquakes, and using only long-period waveforms (as discussed in Polet and Thio (2011)). The USGS also compute moment tensors according to two fundamentally different approaches: one based on filter theory (Sipkin, 1982, 1986, 1994), using body-wave data, and one derived from analysis of the 'W-phase' (Kanamori and Rivera, 2008). A moment tensor calculated by GeoNet from regional data using a method based on that of Dreger and Helmberger (1993) is also given (Ristau, 2008), along with one derived from analysis of InSAR data by Elliott et al. (2012). Clearly, GCMT, USGS CMT and InSAR solutions are in good overall agreement with each other and with our inversion results; the USGS body-wave and W-phase solutions are similar, but with noticeably different orientations and features. The GeoNet source appears strikingly different; this is thought to arise from the regional nature of the determination, and is dominated by the initial rupture, rather than the overall event.

**Table 4**
Source parameters reported for the 3rd September 2010 Darfield earthquake. Global CMT catalogue source from www.globalcmt.org; InSAR source from (Elliott et al., 2012, and pers. comm.). Regional moment tensor from GeoNet, www.geonet.org.nz (Ristau, 2008); USGS Quick CMT solution, body-wave-derived and W-phase-derived moment tensor from earthquake.usgs.gov.

| | GCMT | InSAR | GeoNet | USGS CMT | USGS BW | USGS W |
|---|---|---|---|---|---|---|
| $f_1$ | 0.385 | 0.642 | 1.718 | 0.58 | −0.65 | 0.41 |
| $f_2$ | 0.008 | −0.241 | −0.925 | −0.07 | −0.07 | 0.17 |
| $f_3$ | −0.392 | −0.400 | −0.794 | −0.51 | 0.72 | −0.59 |
| $f_4$ | 0.491 | 0.776 | 3.624 | 0.80 | 0.79 | 1.87 |
| $f_5$ | 0.010 | −0.172 | 3.581 | 0.46 | 0.97 | −0.42 |
| $f_6$ | −3.600 | −3.57 | −4.134 | −3.34 | −2.35 | −3.59 |
| Lat | −43.56 | −43.58 | −43.54 | −43.55 | −43.53 | −43.38 |
| Lon | 172.12 | 172.19 | 172.16 | 171.70 | 172.12 | 172.02 |
| Dep | 12.0 | 5.0 | 8 | 10 | 15 | 15 |
| Time | 0.0 | – | – | −16.4 | 11.9 | 11.9 |

To assess spatial effects, Fig. 12 shows the position of the various sources set out in Tables 3 and 4, along with the latitude and longitude ranges indicated by 1% and 5% thresholds. We see that the various reported locations are reasonably well-clustered – in fact, this event is notable for the level of agreement between source parameters determined by different means. As one might expect, our M84C source inversion recovers a similar location to that obtained by GCMT, as does inversion in PREM; however, inversion in S20RTS leads to a centroid location that agrees significantly less well with other results. Since there is little inherent reason to prefer the low-degree models, we suggest that the close agreement between CMT-inversion results and other methods here may be largely coincidental. We note that the location information provided by the CMT algorithm has often been said to be 'fictitious', prone to systematic error depending on the details of the earth model used: see, for example, Dziewonski and Woodhouse (1983a) or Dziewonski et al. (1987). This is borne out by the results presented in Valentine and Woodhouse (2010). However, we are now in a position to attempt to quantify this.

What error threshold is appropriate for this event? Unfortunately, it seems unlikely that there is a definitive answer to this question, and the user must make their own assessment. We suggest that a reasonable choice would lie somewhere in the range between 1% and 5%, with the spread of inversion results tending to indicate a value at the upper end of this. Comparing the moment tensor components, we can express the ratio of uncertainties $\Delta f_1 : \Delta f_2 : \cdots : \Delta f_6$ based on the ranges in Table 3. For the 1% threshold, we obtain the ratio 1.1 : 1.3 : 1.0 : 2.9 : 3.0 : 1.0, where we have assigned the dominant $f_6$ component unit value. The 5% threshold, on the other hand, yields ratio 0.7 : 0.9 : 1.0 : 3.3 : 2.9 : 1.0. For comparison, the 'standard errors' derived as in Section 3.1, are in the ratio 1.0 : 1.1 : 1.0 : 3.0 : 2.6 : 1.0 – although their numerical values are an order of magnitude, or more, less than those obtained by forward-modelling. However, at low thresholds the two methods partition the uncertainty in a similar manner; when higher thresholds are used, non-linearity becomes more significant, and the two deviate. Thus, we have qualified support for the statement in, for example, Dziewonski et al. (1987) that the standard errors offer a measure of the relative uncertainty in each parameter.

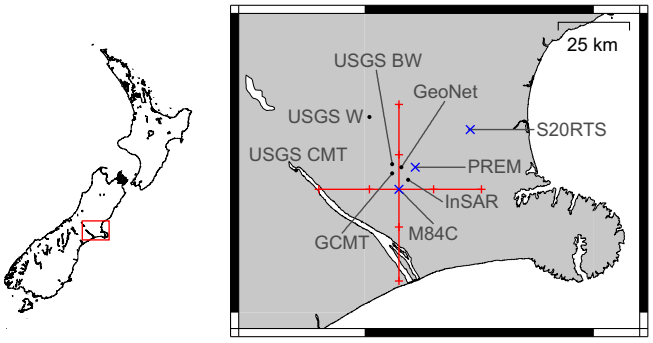


**Fig. 12.** Centroid locations, Darfield earthquake. Black dots denote lateral location of centroid reported by various sources, as in Table 4. Blue crosses denote results from inversion of real data-set in three earth models, as in Table 3. Tick-marks on red lines indicate the extent of the 1% and 5% thresholds set out in Table 3. (For interpretation of the references to colour in this figure legend, the reader is referred to the web version of this article.)

### 5.2. A deep event

It is well-known that the seismic signatures of shallow and deep events are quite different, and thus their behaviour in inversion may also differ. We therefore repeat our analysis for an $M_W$ 6.6 earthquake that occurred at around 13:03 on 18 April 2011 (UTC), on the Kermadec Arc, north of New Zealand; we choose this for its proximity to the Darfield event already discussed, so that effects arising from earth model inaccuracies or station distribution may be broadly comparable between the two. According to the GCMT catalogue, the centroid depth for the event was 99.9 km.

Again, we obtain waveforms from the IRIS/IDA and IRIS/USGS global networks, and process these according to the window definitions set out in Table 1. In practice, we find that the surface wave window type yields very poor results for this particular event, probably on account of its depth: we therefore use only body and mantle waves during inversion. CMT source inversions are performed in three earth models, as before: PREM, M84C and S20RTS; we make use of a triangular source time-function, with a half-width of 4.5 s. The results, along with the 1%, 5% and 10% source parameter ranges evaluated in M84C are shown in Table 5, and the focal mechanisms corresponding to these ranges are given in Fig. 13. For comparison, published source parameters for this event are listed in Table 6, and their locations plotted in Fig. 14 along with our results.

The overall picture appears similar to that for the shallow event: time and location uncertainties remain of a similar magnitude. The ratio of moment tensor uncertainties in this case become 0.8 : 1.4 : 0.8 : 1.4 : 1.0 : 1.2 for the 1% threshold, and 0.8 : 1.3 : 0.8 : 1.4 : 1.0 : 1.2 at the 5% threshold, where we give the dominant $f_5$ component unit weight – remarkably similar. By comparison, the 'standard errors' are in the ratio 0.9 : 1.4 : 1.2 : 1.2 : 1.0 : 1.3, which by our analysis overestimates the uncertainty in the component $f_3$. Again, on balance, we suggest that a threshold value of around 5% is appropriate for this event.

**Table 5**
Results, inversion of real data, deep event. Waveforms for the 18th April 2011 earthquake occurring south of the Kermadec Islands are inverted using the CMT algorithm in earth model M84C, leading to the source denoted 'Best'. The same dataset was also inverted in two further earth models: PREM, and S20RTS. Ranges of source parameters corresponding to 1%, 5% and 10% misfit thresholds are given for the M84C inversion. All moment tensor components are given in units of $10^{25}$ dyn cm – note that this is a factor of 10 different from Table 3. All event times are given in seconds relative the GCMT centroid time for this event, 13:03:07.0 UTC.

| | | 1% Threshold | | 5% Threshold | | 10% Threshold | | | |
|---|---|---|---|---|---|---|---|---|---|
| | Best | Min | Max | Min | Max | Min | Max | PREM | S20RTS |
| $f_1$ | −2.845 | −3.436 | −2.272 | −4.144 | −1.539 | −4.685 | −1.003 | −2.574 | −2.374 |
| $f_2$ | −0.978 | −2.003 | 0.068 | −3.228 | 1.265 | −4.147 | 2.185 | −1.822 | −1.716 |
| $f_3$ | 3.822 | 3.219 | 4.441 | 2.443 | 5.194 | 1.886 | 5.767 | 4.396 | 4.090 |
| $f_4$ | 1.541 | 0.477 | 2.613 | −0.789 | 3.869 | −1.737 | 4.819 | 1.747 | 1.129 |
| $f_5$ | 6.289 | 5.543 | 7.049 | 4.561 | 7.926 | 3.991 | 8.588 | 6.046 | 5.142 |
| $f_6$ | 1.234 | 0.332 | 2.136 | −0.750 | 3.221 | −1.564 | 4.032 | 1.562 | 1.380 |
| Lat | −34.28 | −34.48 | −34.07 | −34.74 | −33.82 | −34.94 | −33.64 | −34.36 | −34.11 |
| Lon | 180.06 | 179.95 | 180.19 | 179.78 | 180.35 | 179.65 | 180.46 | 180.12 | 180.34 |
| Dep | 94.17 | 85.23 | 104.13 | 76.43 | 116.24 | 69.27 | 126.17 | 101.23 | 110.10 |
| Time | −1.4 | −2.9 | 0.3 | −5.2 | 2.5 | −6.9 | 4.1 | −2.9 | 0.9 |
| $m^2_{\min}$ | 0.435 | | | | | | | 0.450 | 0.471 |

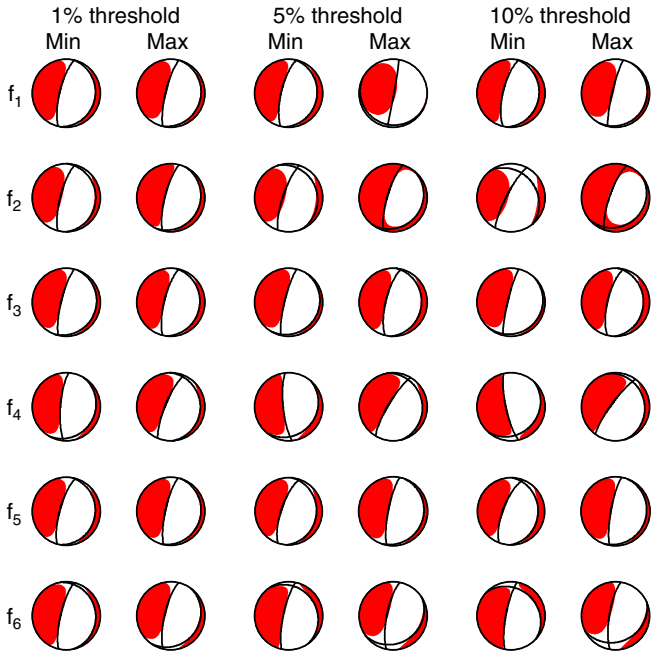


**Fig. 13.** Focal mechanisms corresponding to misfit thresholds, deep event. 'Beachballs' corresponding to the sources yielding upper and lower bounds for each parameter according to misfit thresholds of 1%, 5% and 10%, as set out in Table 5. Best-fitting double couple is overlaid in black for each mechanism.

**Table 6**
Source parameters reported for the 18 April 2011 event that occurred south of the Kermadec Islands. Global CMT catalogue source from www.globalcmt.org; regional moment tensor from GeoNet, www.geonet.org.nz. USGS CMT and W-phase solutions from earthquakes.usgs.gov.

| | GCMT | GeoNet | USGS CMT | USGS W |
|---|---|---|---|---|
| $f_1$ | −3.040 | −3.008 | −3.64 | −4.50 |
| $f_2$ | −1.310 | −0.155 | −0.59 | 0.88 |
| $f_3$ | 4.350 | 3.163 | 4.23 | 3.61 |
| $f_4$ | 2.050 | 3.455 | 2.62 | 1.99 |
| $f_5$ | 6.560 | 6.894 | 8.60 | 7.57 |
| $f_6$ | 0.985 | 2.070 | 1.30 | 1.03 |
| Lat | −34.34 | −34.29 | −34.30 | −34.12 |
| Lon | 179.87 | 180.97 | 180.38 | 170.19 |
| Dep | 86.00 | 99 | 62 | 90 |
| Time | 0.0 | – | 16.6 | −3.0 |

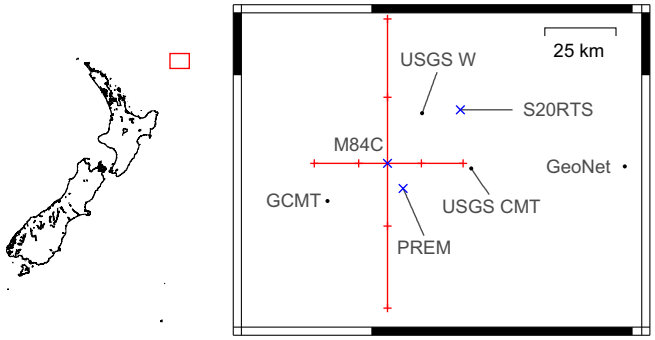


**Fig. 14.** Centroid locations, earthquake south of the Kermadec Islands. Black dots denote published locations as reported in Table 6; blue crosses denote results of inversion of real data in different Earth models, as set out in Table 5. Tick-marks on red lines indicate the lateral extent of the 1% and 5% thresholds given in that table. Note that the horizontal and vertical extent of the main map in this figure is equivalent, in kilometres, to that shown in Fig. 12. (For interpretation of the references to colour in this figure legend, the reader is referred to the web version of this article.)

## 6. A comparison with linear inverse theory

Our approach has been based upon evaluating the form of the misfit surface in the region of the best-fitting solution by explicitly computing the wavefield. However, by making use of the linear approximation in Eq. (3), it is possible to estimate the misfit due to a perturbation away from the minimum. For a given dataset, **d**, this allows Eq. (2) to be re-written in the form

$$\begin{aligned} m^2(\mathbf{m}+\Delta\mathbf{m}) &= \frac{[\mathbf{d}-\mathbf{s}(\mathbf{m}+\Delta\mathbf{m})]^{\mathrm{T}}[\mathbf{d}-\mathbf{s}(\mathbf{m}+\Delta\mathbf{m})]}{\mathbf{d}^{\mathrm{T}}\mathbf{d}} \\ &= \frac{[\mathbf{d}-\mathbf{s}(\mathbf{m})-\mathbf{A}\Delta\mathbf{m}]^{\mathrm{T}}[\mathbf{d}-\mathbf{s}(\mathbf{m})-\mathbf{A}\Delta\mathbf{m}]}{\mathbf{d}^{\mathrm{T}}\mathbf{d}} \\ &= \frac{1}{\mathbf{d}^{\mathrm{T}}\mathbf{d}}\left\{[\mathbf{d}-\mathbf{s}(\mathbf{m})]^{\mathrm{T}}[\mathbf{d}-\mathbf{s}(\mathbf{m})]-2\Delta\mathbf{m}^{\mathrm{T}}\mathbf{A}^{\mathrm{T}}[\mathbf{d}-\mathbf{s}(\mathbf{m})]+\Delta\mathbf{m}^{\mathrm{T}}\mathbf{A}^{\mathrm{T}}\mathbf{A}\Delta\mathbf{m}\right\}, \end{aligned} \tag{11}$$

where **A** is the matrix of partial derivatives evaluated at **m**. Expressing the quantity $\mathbf{d}-\mathbf{s}(\mathbf{m})$ as **e** for brevity, this implies that

$$m^2(\mathbf{m}+\Delta\mathbf{m}) = \left[1+\frac{\Delta\mathbf{m}^{\mathrm{T}}\mathbf{A}^{\mathrm{T}}\mathbf{A}\Delta\mathbf{m}-2\Delta\mathbf{m}^{\mathrm{T}}\mathbf{A}^{\mathrm{T}}\mathbf{e}}{\mathbf{e}^{\mathrm{T}}\mathbf{e}}\right]m^2(\mathbf{m}). \tag{12}$$

The quantities $\mathbf{A}^{\mathrm{T}}\mathbf{A}$ and $\mathbf{A}^{\mathrm{T}}\mathbf{e}$ appear in the least-squares algorithm, Eq. (5), and are therefore computed during source inversion. As a result, once the minimum-misfit solution has been obtained, it is

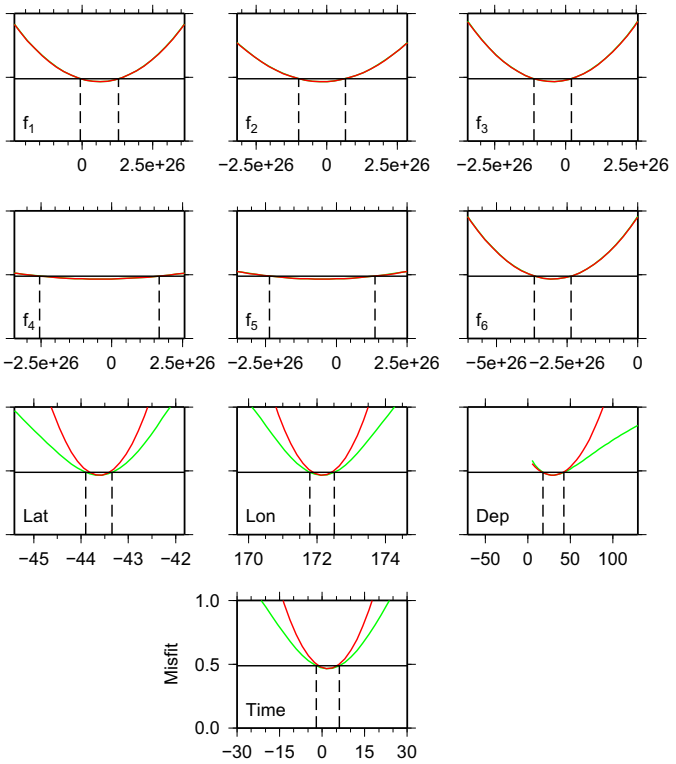


**Fig. 15.** Comparison with predictions of linear inverse theory. Green curves show misfit using approximate synthetic seismograms in M84C for the Darfield event, as already discussed. Red curves represent the misfit predicted by assuming seismograms to depend linearly on source parameters close to the minimum, as set out in Section 6. For the six moment tensor components, both curves coincide exactly, as predicted by normal mode theory. The 5% misfit threshold is illustrated, estimated from the green curves, and can be seen to broadly represent the point at which the two curves diverge. Note that scales differ between this figure and earlier examples. (For interpretation of the references to colour in this figure legend, the reader is referred to the web version of this article.)

trivial to use Eq. (12) to estimate the misfit for any source close to the minimum.

Fig. 15 compares the misfit curve obtained using Eq. (12) to that obtained by the forward-modelling approach already discussed, for the Darfield event. The two curves agree exactly for the six moment tensor components, as the seismogram is exactly linear in these. For spatio-temporal components, the two curves differ due to the inherent non-linearity ignored in Eq. (12), which typically over-estimates misfit. However, close to the minimum, agreement is good – and for reasonable values of $\phi$, the two curves will lead to similar parameter ranges. Thus, if the quantities $\mathbf{A}^T\mathbf{A}, \mathbf{A}^T\mathbf{e}$ and $\mathbf{e}^T\mathbf{e}$ corresponding to the minimum-misfit solution are available, it is particularly straightforward to estimate plausible parameter ranges, or to assess the extent to which some other source estimate, $\mathbf{m}'$, may be compatible with the CMT solution.

## 7. Conclusions

We have set out a method by which researchers may estimate the overall waveform effect of small changes in source parameters, and thus estimate the uncertainties on moment tensors and location co-ordinates derived by the CMT algorithm. The user must make some assessment of the overall accuracy of their synthetic waveforms, based on their confidence in the earth model and modelling strategy used; unfortunately, we do not yet have sufficient understanding of the errors in earth models and their propagation to compute this directly. We suggest that this approach has a sounder basis than an analysis based on Gaussian statistics.

If the user has access to the quantities $\mathbf{A}^T\mathbf{A}, \mathbf{A}^T[\mathbf{d}-\mathbf{s}(\mathbf{m})]$ and $[\mathbf{d}-\mathbf{s}(\mathbf{m})]^T[\mathbf{d}-\mathbf{s}(\mathbf{m})]$ for the best-fitting source, $\mathbf{m}$, the misfit for sources close to this can be estimated straightforwardly as set out in Section 6, and parameter ranges corresponding to low values of $\phi$ may be estimated. For researchers performing their own source determinations, this may be an effective route to assessing uncertainty. It might also be feasible for maintainers of CMT catalogues to publish these quantities: the dimension of the matrices involved is small. Maintainers could also consider providing more detailed information about the datasets used for each determination, although finding an effective format for this may present technical challenges.

If this information is not available, or users wish to allow for larger changes in source parameters, for which the linear approximation is not valid, we have shown that forward modelling will allow the calculation of curves showing the tradeoff between individual parameters and misfit. The computational cost of this procedure is not high: broadly, it amounts to another iteration of the CMT algorithm per source parameter, and can be readily distributed over the nodes of a computational cluster. It requires the user to have access only to a method for computing synthetic seismograms, although for fully self-consistent results, the experimental setup must be identical to that used for source determination.

In this paper, we have considered only two events, and we are wary of drawing too many generalisations. However, our observations here support a number of points made elsewhere in the CMT literature, and these may be usefully re-stated:

1. The CMT algorithm allows the calculation of the set of source parameters that allow a particular modelling approach to best explain a particular dataset in a given earth model.
2. Inadequacies in earth models and modelling approaches lead to different results in different frequency bands; combining datasets leads to a solution that 'averages' these.
3. Structural effects may introduce bias into results, particularly for parameters describing spatial location.
4. Standard errors obtained by statistical analysis significantly underestimate the true scale of uncertainty, particularly where datasets are large – as is typically the case in recent routine determinations. However, they may provide a reasonable estimate of the relative uncertainties in parameters.
5. For shallow sources, components $f_4$ and $f_5$ are extremely poorly constrained.

Furthermore, it is apparent that moderate changes to source parameters may be possible without significant effect on the overall waveform misfit.

Perhaps the most important conclusion to be drawn from our current work is that the best-fitting source parameters depend strongly on the details of the dataset, earth model and modelling approach used. This effect was seen in Valentine and Woodhouse (2010), and we believe it is clearer in the current work: one should not use source parameters as a basis for modelling without ensuring that the manner of their determination is compatible with the intended use. Differences in earth model or waveform frequency band should be approached with particular caution; however, even differences in the particular stations used may have consequences. Unfortunately, catalogue sources are rarely accompanied by sufficient information to allow the user to make this assessment. We therefore suggest that where detailed inferences are to be made based on synthetic waveforms, or where self-consistency is otherwise important, researchers should give serious consideration to performing their own source determinations.

## Acknowledgements

The authors would like to thank John Woodhouse for providing us with his source code, and for his input in the early stages of this research. We also thank Theo van Zessen for taking care of The Stig, John Elliott for providing additional details of his InSAR-derived rupture model for the Darfield earthquake, and John Ristau for providing information on the GeoNet regional moment tensor for this event. APV is grateful to Tom O'Toole for many helpful discussions, and we wish to acknowledge the participants in the 'Uncertainty Analysis in Geophysical Inverse Problems' workshop held in Leiden in November 2011, which helped shape the form of this paper. Seismic data used in this study was obtained from the IRIS data centre, www.iris.edu, and APV is supported by QUEST, an Initial Training Network funded under the 'Marie Curie Actions' of the European Commission (Grant 238007). Finally, we are grateful to the editor, George Helffrich, and to Göran Ekström and an anonymous reviewer for their comments and suggestions.

## Appendix A. The CMT source representation

Hooke's Law states that for small deformations, stress (**T**) and strain (**s**) are linearly related. In general, this may be expressed (e.g. Biot, 1965; Dziewonski and Woodhouse, 1983b)

$$T_{ij} = d_{ijkl}\partial_l s_k, \tag{A.1}$$

where we have adopted the Einstein convention of summation over repeated indices, and where **d** represents the elasticity tensor of the material. Of course, deformations may not be entirely elastic, and Backus and Mulcahy (1976) introduced the *stress glut*, $\boldsymbol{\Gamma}$, representing the departure from Hooke's law in a given case. This is *defined* by

$$T_{ij} = d_{ijkl}\partial_l s_k - \Gamma_{ij}. \tag{A.2}$$

The equations of motion governing the response of the Earth to some seismic event then take the form

$$\rho_0 \ddot{s}_i = \mathcal{H} s_i - \partial_j \Gamma_{ij}, \tag{A.3}$$

where $\mathcal{H}$ represents a linear integro-differential operator (see, for example, Dziewonski and Woodhouse, 1983b; Woodhouse and Deuss, 2007). The stress glut therefore defines an equivalent body force for the event

$$\mathfrak{f}_i = -\partial_j \Gamma_{ij} \tag{A.4}$$

and must be symmetric for an indigenous event.

For any given stress glut tensor, $\boldsymbol{\Gamma}$, we can define spatio-temporal glut moments (Backus, 1977),

$$M_{ij} = \int_{t_1}^{t_2} \int_{V_S} \dot{\Gamma}_{ij}(\mathbf{x}', t')\, \mathrm{d}^3x'\, \mathrm{d}t', \tag{A.5}$$

$$\Lambda_{ijk}(\mathbf{x}) = \int_{t_1}^{t_2} \int_{V_S} (x'_k - x_k)\dot{\Gamma}_{ij}(\mathbf{x}', t')\, \mathrm{d}^3x'\, \mathrm{d}t', \tag{A.6}$$

$$H_{ij}(t) = \int_{t_1}^{t_2} \int_{V_S} (t' - t)\dot{\Gamma}_{ij}(\mathbf{x}', t')\, \mathrm{d}^3x'\, \mathrm{d}t'. \tag{A.7}$$

where a dot is used to denote the *material* time derivative of the stress glut, and **x** and $t$ represent the spatial and temporal components, respectively. The domain of integration, $V_S$, is the entire 'source region' in which the stress glut is non-zero; $t_1$ and $t_2$ are chosen to span the time over which the source acts. **M** is often referred to as 'the' moment tensor for the event, and it is this quantity that the CMT algorithm seeks to determine, along with the spatio-temporal centroid location $(\mathbf{x}_c, t_c)$. This is defined to be the point at which the sum of squares of $\boldsymbol{\Lambda}$ and **H** are minimised

$$\frac{\partial}{\partial x_k}\left[\Lambda_{ijk}(\mathbf{x})\Lambda_{ijk}(\mathbf{x})\right]_{\mathbf{x}=\mathbf{x}_c} = 0, \tag{A.8}$$

$$\frac{\partial}{\partial t}\left[H_{ij}(t)H_{ij}(t)\right]_{t=t_c} = 0. \tag{A.9}$$

In practice, $t_c$ is typically specified as a time-shift relative to some reference time. Combining Eqs. (A.5)–(A.9), it is straightforward to show that

$$\Lambda_{ijk}(\mathbf{x}_c)M_{ij} = 0 \tag{A.10}$$

$$H_{ij}(t_c)M_{ij} = 0, \tag{A.11}$$

and therefore that the second glut moments $\Lambda$ and **H** must vanish at the centroid point.

Since $\boldsymbol{\Gamma}$ is symmetric, **M** must also be symmetric. With three spatial dimensions, this implies that the moment tensor has six independent components; it can therefore be described by a six-element *source vector*, **f**. Working in spherical polar co-ordinates $(r, \theta, \phi)$, we therefore have

$$\mathbf{M} = \begin{pmatrix} M_{rr} & M_{r\theta} & M_{r\phi} \\ M_{\theta r} & M_{\theta\theta} & M_{\theta\phi} \\ M_{\phi r} & M_{\phi\theta} & M_{\phi\phi} \end{pmatrix} = \begin{pmatrix} f_1 & f_4 & f_5 \\ f_4 & f_2 & f_6 \\ f_5 & f_6 & f_3 \end{pmatrix}. \tag{A.12}$$

Thus, our description of the seismic source requires ten parameters, leading to the CMT vector set out in Eq. (1). It should be apparent that modelling the source in this manner is essentially a first-order approximation: we are neglecting information on the spatio-temporal variation of the source, as encapsulated in the higher glut moments.

## Appendix B. Generating random sources

The algorithm used to generate a set of random source parameters 'close' to some true set $\mathbf{m}_{\text{true}}$ is straightforward. We use $\mathcal{U}(a, b)$ to denote a random number drawn from a uniform distribution, in the range $[a, b]$. In addition, we define $f_{\max}$ to be the largest component of the moment tensor

$$f_{\max} = \max\left(|f_1^{\text{true}}|, |f_2^{\text{true}}|, \ldots, |f_6^{\text{true}}|\right) \tag{B.1}$$

The ten components of a random source with vanishing isotropic part may then be expressed

$$f_{1,2,4,\ldots,6} = \mathcal{U}\left(f_{1,2,4,\ldots,6}^{\text{true}} - w_f f_{\max}, f_{1,2,4,\ldots,6}^{\text{true}} + w_f f_{\max}\right) \tag{B.2}$$

$$f_3 = -f_1 - f_2 \tag{B.3}$$

$$z_c = \mathcal{U}\left(\max\left(z_c^{\min}, z_c^{\text{true}} - w_z\right), z_c^{\text{true}} + w_z\right) \tag{B.4}$$

$$\vartheta_c = \mathcal{U}\left(\vartheta_c^{\text{true}} - \frac{180\, w_k}{\pi R_\oplus}, \vartheta_c^{\text{true}} + \frac{180\, w_k}{\pi R_\oplus}\right) \tag{B.5}$$

$$\varphi_c = \mathcal{U}\left(\varphi_c^{\text{true}} - \frac{180\, w_k}{\pi R_\oplus \cos\vartheta_c^{\text{true}}}, \varphi_c^{\text{true}} + \frac{180\, w_k}{\pi R_\oplus \cos\vartheta_c^{\text{true}}}\right) \tag{B.6}$$

$$t_c = \mathcal{U}(-w_t, w_t) \tag{B.7}$$

where $R_\oplus$ represents the radius of the Earth (taken to be 6371 km), $z_c^{\min} \geqslant 0$ provides a constraint on the minimum permissible event depth (we adopt $z_c^{\min} = 5$ km), and where the various $w$ parameters control the width of each distribution. In addition, we require that

$$f_3^{\text{true}} - w_f f_{\max} \leqslant f_3 \leqslant f_3^{\text{true}} + w_f f_{\max}, \tag{B.8}$$

and we discard and regenerate any source for which this does not hold. In this paper, we use $w_f = 0.5, w_z = 50$ km, $w_k = 100$ km and $w_t = 15$ s, although such choices are obviously somewhat arbitrary.

## References

Backus, G., 1977. Interpreting the seismic glut moments of total degree two or less. Geophysical Journal of the Royal Astronomical Society 51, 1–25.

Backus, G., Mulcahy, M., 1976. Moment tensors and other phenomenological descriptions of seismic sources I. Continuous displacements. Geophysical Journal of the Royal Astronomical Society 46, 341–361.

Biot, M., 1965. Mechanics of Incremental Deformations. John Wiley & Sons, New York.

Crotwell, H., Owens, T., Ritsema, J., 1999. The TauP toolkit: flexible seismic travel-time and raypath utilities. Seismological Research Letters 70, 154–160.

Dreger, D., Helmberger, D., 1993. Determination of source parameters at regional distances with three-component sparse network data. Journal of Geophysical Research 98, 8107–8125.

Durek, J., Ekström, G., 1996. A radial model of anelasticity consistent with long-period surface-wave attenuation. Bulletin of the Seismological Society of America 86, 144–158.

Dziewonski, A., Anderson, D., 1981. Preliminary reference Earth model. Physics of the Earth and Planetary Interiors 25, 297–356.

Dziewonski, A., Chou, T.A., Woodhouse, J., 1981. Determination of earthquake source parameters from waveform data for studies of global and regional seismicity. Journal of Geophysical Research 86, 2825–2852.

Dziewonski, A., Ekström, G., Franzen, J., Woodhouse, J., 1987. Centroid-moment tensor solutions for January–March 1986. Physics of the Earth and Planetary Interiors 45, 1–10.

Dziewonski, A., Ekström, G., Salganik, M., 1992. Centroid-moment tensor solutions for July–September 1991. Physics of the Earth and Planetary Interiors 72, 1–11.

Dziewonski, A., Woodhouse, J., 1983a. An experiment in the systematic study of global seismicity: centroid-moment tensor solutions for 201 moderate and large earthquakes of 1981. Journal of Geophysical Research 88, 3247–3271.

Dziewonski, A., Woodhouse, J., 1983b. Studies of the seismic source using normal-mode theory. In: Kanamori, H., Boschi, E. (Eds.), Earthquakes: Observation, Theory, and Interpretation. North-Holland, Amsterdam, pp. 45–137, Proceedings of the International School of Physics Enrico Fermi.

Dziewonski, A., Woodward, R., 1992. Acoustic imaging at the planetary scale. In: Emert, H., Harjes, H.P. (Eds.), Acoustical Imaging, vol. 19. Plenum Press, New York, pp. 785–797.

Ekström, G., 2011. A global model of Love and Rayleigh surface wave dispersion and anisotropy, 25–250 s. Geophysical Journal International.

Ekström, G., Dziewonski, A., Maternovskaya, N., Nettles, M., 2005. Global seismicity of 2003: centroid-moment-tensor solutions for 1087 earthquakes. Physics of the Earth and Planetary Interiors 148, 327–351.

Ekström, G., Nettles, M., Dziewonski, A., 2012. The Global CMT Project 2004–2010: centroid-moment tensors for 13,017 earthquakes. Physics of the Earth and Planetary Interiors.

Elliott, J., Nissen, E., England, P., Jackson, J., Lamb, S., Li, Z., Oehlers, M., Parsons, B., 2012. Slip in the 2010–2011 Canterbury earthquakes, New Zealand. Journal of Geophysical Research.

Elliott, J., Walters, R., England, P., Jackson, J., Li, Z., Parsons, B., 2010. Extension on the Tibetan plateau: recent normal faulting measured by InSAR and body wave seismology. Geophysical Journal International 183, 503–535.

Ferreira, A., Woodhouse, J., 2006. Long period seismic source inversions using global tomographic models. Geophysical Journal International 166, 1178–1192.

Helffrich, G., 1997. How good are routinely determined focal mechanisms? Empirical statistics based on a comparison of Harvard, USGS and ERI moment tensors. Geophysical Journal International 131, 741–750.

Hjörleifsdóttir, V., Ekström, G., 2010. Effects of three-dimensional Earth structure on CMT earthquake parameters. Physics of the Earth and Planetary Interiors 179, 178–190.

Jackson, D., 1976. Most squares inversion. Journal of Geophysical Research 81, 1027–1030.

Julian, B., Miller, A., Foulger, G., 1998. Non-double-couple earthquakes 1: theory. Reviews of Geophysics 36, 525–549.

Kagan, Y., 2003. Accuracy of modern global earthquake catalogs. Physics of the Earth and Planetary Interiors 135, 173–209.

Kanamori, H., Rivera, L., 2008. Source inversion of W phase: speeding up seismic tsunami warning. Geophysical Journal International 175, 222–238.

Komatitsch, D., Erlebacher, G., Göddeke, D., Michéa, D., 2010. High-order finite-element seismic wave propagation modeling with MPI on a large GPU cluster. Journal of Computational Physics 229, 7692–7714.

Komatitsch, D., Tromp, J., 2002a. Spectral-element simulations of global seismic wave propagation I: validation. Geophysical Journal International 149, 390–412.

Komatitsch, D., Tromp, J., 2002b. Spectral-element simulations of global seismic wave propagation II. Three-dimensional models, oceans, rotation and self-gravitation. Geophysical Journal International 150, 303–318.

Langbein, J., Johnson, H., 1997. Correlated errors in geodetic time series: implications for time-dependent deformation. Journal of Geophysical Research 102, 591–603.

Liu, Q., Polet, J., Komatitsch, D., Tromp, J., 2004. Spectral-element moment tensor inversions for earthquakes in southern California. Bulletin of the Seismological Society of America 94, 1748–1761.

Lohmann, R., Simons, M., 2005. Some thoughts on the use of InSAR data to constrain models of surface deformation: noise structure and data downsampling. Geochemistry, Geophysics, and Geosystems 6.

Madriaga, R., 2007. Seismic source theory. In: Kanamori, H. (Ed.), Earthquake seismology, Elsevier, volume 4 of Treatise on Geophysics, pp. 59–82 (Chapter 2).

Meju, M., Hutton, V., 1992. Iterative most-squares inversion: application to magnetotelluric data. Geophysical Journal International 108, 758–766.

Menke, W., 1989. Geophysical Data Analysis: Discrete Inverse Theory. Academic Press, New York.

Miller, A., Foulger, G., Julian, B., 1998. Non-double-couple earthquakes 2: observations. Reviews of Geophysics 36, 551–568.

Mosegaard, K., Tarantola, A., 2002. Probabilistic approach to inverse problems. In: International Handbook of Earthquake and Engineering Seismology, Academic Press, pp. 237–265.

Panning, M., Romanowicz, B., 2006. A three-dimensional radially anisotropic model of shear velocity in the whole mantle. Geophysical Journal International 167, 361–379.

Polet, J., Thio, H., 2011. Rapid calculation of a Centroid Moment Tensor and waveheight predictions around the north Pacific for the 2011 off the Pacific coast of Tohoku earthquake. Earth Planets Space 63, 541–545.

Ristau, J., 2008. Implementation of routine regional moment tensor analysis in New Zealand. Seismological Research Letters 79, 400–415.

Ritsema, J., Deuss, A., van Heijst, H., Woodhouse, J., 2011. S40RTS: a degree-40 shear-velocity model for the mantle from new Rayleigh wave dispersion, teleseismic traveltime and normal-mode splitting function measurements. Geophysical Journal International 184, 1223–1236.

Ritsema, J., van Heijst, H., Woodhouse, J., 2004. Global transition zone tomography. Journal of Geophysical Research 109.

Romanowicz, B., 1988. Asymptotic theory of normal modes and surface waves. In: Desaubies, Y., Tarantola, A., Zinn-Justin, J. (Eds.), Oceanographic and Geophysical Tomography. North-Holland, Amsterdam, pp. 135–158 (Chapter 3).

Sipkin, S., 1982. Estimation of earthquake source parameters by the inversion of waveform data: synthetic waveforms. Physics of the Earth and Planetary Interiors 30, 242–259.

Sipkin, S., 1986. Estimation of earthquake source parameters by inversion of waveform data: global seismicity, 1981–1983. Bulletin of the Seismological Society of America 76, 1515–1541.

Sipkin, S., 1994. Rapid determination of global moment-tensor solutions. Geophysical Research Letters 21, 1667–1670.

Sipkin, S., Person, W., Presgrave, B., 2000. Earthquake bulletins and catalogs at the USGS National Earthquake Information Center. IRIS Newsletter, 2–4.

Smith, G., Ekström, G., 1997. Interpretation of earthquake epicenter and CMT centroid locations, in terms of rupture length and direction. Physics of the Earth and Planetary Interiors 102, 123–132.

Squires, G., 2001. Practical Physics. Cambridge University Press, Cambridge.

Tarantola, A., 1987. Inverse Problem Theory. Elsevier.

Tarantola, A., Valette, B., 1982. Generalized nonlinear inverse problems solved using the least squares criterion. Reviews of Geophysics and Space Physics 20, 219–232.

Valentine, A., Woodhouse, J., 2010. Reducing errors in seismic tomography: combined inversion for sources and structure. Geophysical Journal International 180, 847–857.

Weston, J., Ferreira, A., Funning, G., 2011. Global compilation of InSAR earthquake source models: 1. Comparisons with seismic catalogs. Journal of Geophysical Research.

Woodhouse, J., Deuss, A., 2007. Earth's free oscillations. In: Romanowicz, B., Dziewoński, A. (Eds.), Seismology and structure of the Earth. Elsevier, Amsterdam, volume 1 of Treatise on Geophysics, pp. 31–65 (Chapter 2).

Woodhouse, J., Dziewonski, A., 1984. Mapping the upper mantle: three-dimensional modelling of Earth structure by inversion of seismic waveforms. Journal of Geophysical Research 89, 5953–5986.

Yagi, Y., Fukahata, Y., 2008. Importance of covariance components in inversion analyses of densely sampled observed data: an application to waveform data inversion for seismic source processes. Geophysical Journal International 175, 215–221.

Yagi, Y., Fukahata, Y., 2011. Introduction of uncertainty of Green's function into waveform inversion for seismic source processes. Geophysical Journal International 186, 711–720.